Research Article Vol. 34, No. 3 / 9 Feb 2026 / Optics Express 4270
Optics EXPRESS

Adaptive-sign CMA for continuous-variable quantum key distribution under high-speed polarization disturbances

Si Qiu,[1,2] Yan Tian,[3] Shaobo Ren,[1,2] Zehong Wang,[1,2] Shuaishuai Liu,[1,2] Jiaxiang Song,[4] Zhenguo Lu,[1,2,6] and Yongmin Li[1,2,5,7]

[1]State Key Laboratory of Quantum Optics Technologies and Devices, Institute of Opto-Electronics, Shanxi University, Taiyuan 030006, China
[2]Collaborative Innovation Center of Extreme Optics, Shanxi University, Taiyuan 030006, China
[3]School of Information and Communication Engineering, North University of China, Taiyuan 030051, China
[4]College of Physics and Electronic Engineering, Shanxi University, Taiyuan 030006, China
[5]Hefei National Laboratory, Hefei 230088, China
[6]zglu@sxu.edu.cn
[7]yongmin@sxu.edu.cn

Abstract: Polarization disturbance in long distance single-mode fiber is detrimental to both the classical and quantum communications. Here we proposes an adaptive-sign constant modulus algorithm (AS-CMA) using an error-driven adaptive step size and a sign-based weight update, which jointly enhances the performance while reducing the computational complexity of the conventional CMA. We validate the algorithm on a continuous-variable quantum key distribution system. Simulation results show that under 10 Mrad/s polarization disturbance, the secret key rate achieved using AS-CMA method only decreases by 12.9% at 25 km single-mode fiber. Robust polarization recovery and positive secret key rate can be maintained even under extreme 43 Mrad/s lightning transients. Our results provides an efficient, low-complexity solution for polarization recovery in CV-QKD system.

1. Introduction

The rapid advancement of information technology has greatly impacted modern society, driving ever-increasing demands for higher transmission capacity, reliability, and security in communication systems. Against this backdrop, quantum key distribution (QKD), which offer information-theoretical security has attracted intense attractions [1,2].

Single-mode fiber has low transmission loss at telecom band of 1.5 micron and provides a superior transmission media for QKD. However, the polarization state of the quantum signals suffer from inevitable disturbances in long distance single-mode fiber owing to the intrisic refractive index inhomogeneity, temperature fluctuations, and mechanical stress [3–6]. Studies indicate that the rate of polarization state change can reach 280 krad/s in laboratory settings and 1 Mrad/s in natural environments [7,8]. Under extreme conditions such as a direct lighting strike, the instantaneous rate can even reach 43 Mrad/s [7–9]. Such rapid polarization disturbance can lead to an increased bit error rates in classical communication systems [10]. In continuous-variable quantum key distribution (CV-QKD) systems [11–22], it directly impacts the channel transmittance and excess noise, which in turn degrades the secret key rate (SKR) [23]. Therefore, the development of efficient polarization recovery techniques are crucial.

Recently, several works have been reported for polarization recovery in CV-QKD, including the CMA with constant step size [15,24], Kalman filter [25,26], unscented Kalman filter [27,28],

#586369 https://doi.org/10.1364/OE.586369
Journal © 2026 Received 3 Dec 2025; revised 6 Jan 2026; accepted 11 Jan 2026; published 28 Jan 2026

Optics EXPRESS

inverse Jones matrix by orthogonal pilot tones [29]. Among these, high-speed CV-QKD with polarization multiplexing using the CMA algorithm were reported [24]. It was shown that Kalman filter algorithm can resist the polarization state rotation at 1 krad/s [25]. A Stokes space-based polarization tracking algorithm enables experimental polarization state tracking rate of 12.57 krad/s [29]. Despite its superior performance, Kalman filter algorithm imposes high demands on the real-time processing capability due to its complex iterative computational structures. Meanwhile, the inverse Jones matrix method relies on orthogonal pilot tones, the additional pilot tone subsequently reduces the effective number of bits of the ADC for the weak quantum signals. In contrast, CMA based on the MIMO structure is relatively simple and require fewer computing resources. However, conventional CMA suffers from limited equalization capability and slow convergence speed [30,31].

In this paper, we proposes an adaptive-sign CMA (AS-CMA). Our approach achieves a significant enhancement in both the convergence speed and steady-state performance of the polarization equalization, while preserving the low-complexity benefit of the MIMO structure. This is enabled through the introduction of an error-driven adaptive step size, coupled with a sign-based weight update mechanism. We validate the algorithm in a simulated 16-amplitude and phase shifting (APSK) CV-QKD system. Under 10 Mrad/s polarization disturbance, the simulations show that SKR of 5.38 Mbps can be obtained over 25 km single-mode fiber which represents a fourfold performance improvement over the conventional CMA (C-CMA). Even under extreme conditions of a 43 Mrad/s lightning disturbance, the CV-QKD system can still remain positive SKR.

2. Model of the AS-CMA

2.1. Rotation of polarization state in fiber

Polarization impairments in fiber comprise three main effects: rotation of state of polarization (RSOP), polarization mode dispersion, and polarization-dependent loss. In this paper, we focus on the RSOP, and in this case a 2×2 Jones matrix with three independent parameters is sufficient to characterize the RSOP effect of an optical fiber channel [5].

$$J(\xi,\eta,\kappa)=\begin{pmatrix}\cos\kappa e^{j\xi} & -\sin\kappa e^{j\eta}\\ \sin\kappa e^{-j\eta} & \cos\kappa e^{-j\xi}\end{pmatrix}, \tag{1}$$

where ξ and η are the phase angles, and κ is the amplitude ratio angle. By using Eq. (1), the output state of polarization (SOP) through a optical fiber channel can be given by

$$E_{out}=JE_{in}=\begin{pmatrix}\cos\kappa e^{j\xi} & -\sin\kappa e^{j\eta}\\ \sin\kappa e^{-j\eta} & \cos\kappa e^{-j\xi}\end{pmatrix}\begin{bmatrix}E_{x,in}\\ E_{y,in}\end{bmatrix}. \tag{2}$$

The probability density function (PDF) of the polarization state change rate approximately conforms to a Rayleigh distribution [32], as shown in Fig. 1(a):

$$p_v(v)=\left(2v/v_{rms}^2\right)e^{-v^2/v_{rms}^2}, \tag{3}$$

where v_{rms} is the root mean square (RMS) speed. Approximate calculations show that the maximum polarization rotation rate is about three times the value of RMS.

In this study, to evaluate the recovery capability of the CMA algorithm against extreme physical disturbances, we also consider the ultra-fast polarization transients induced by direct lightning strikes on composite overhead ground wire (OPGW)-based optical fiber channels. When a direct lightning current travels through the helical metal structure of the OPGW, it generates a

Optics EXPRESS

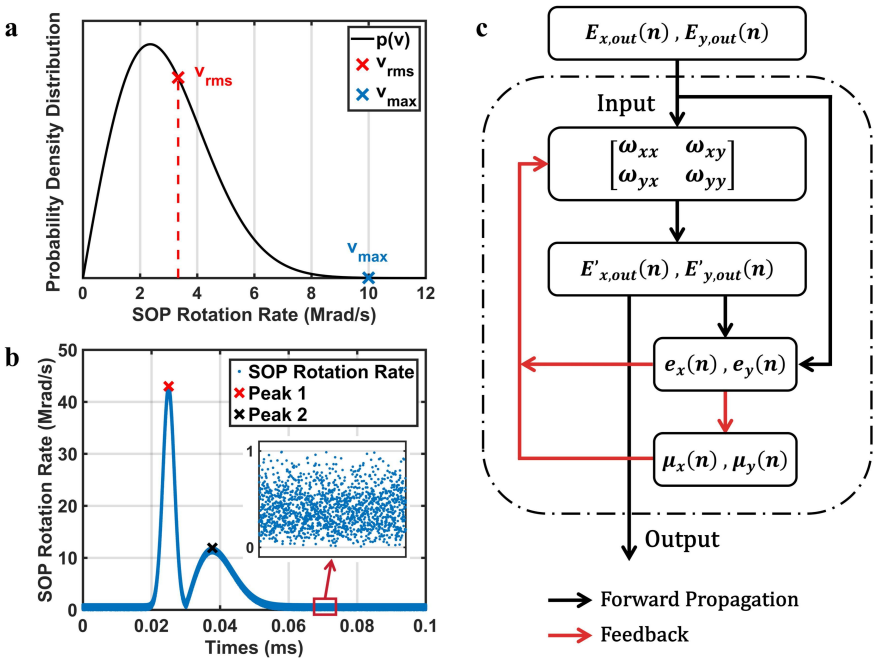

Fig. 1. (a) Probability density distribution of the SOP rotation rate at a maximum rate of 10 Mrad/s, the distribution follows a Rayleigh distribution; (b) SOP rotational rate curve versus time during a lightning strike; (c) AS-CMA algorithm flowchart.

strong magnetic field along the optical fiber's axis. Due to the Faraday magneto-optic effect, this magnetic field introduces a time-varying pure rotational perturbation to the SOP of the optical fields in the transmission fiber. The current waveform of a single lightning strike typically presents two peaks and a characteristic sharp rise and fall, with the highest peak reaching 43 Mrad/s [7,8], as shown in Fig. 1(b).

2.2. AS-CMA algorithm

The essence of polarization demultiplexing is equivalent to estimate the inverse matrix U of the transmission channel's Jones matrix J,

$$U = J^{-1} = \begin{bmatrix} \omega_{xx} & \omega_{xy} \\ \omega_{yx} & \omega_{yy} \end{bmatrix}, \tag{4}$$

by applying the inverse Jones matrix U, The original signal can be reconstructed from the received signal

$$\begin{bmatrix} E'_{x,out} \\ E'_{y,out} \end{bmatrix} = U \begin{bmatrix} E_{x,out} \\ E_{y,out} \end{bmatrix} = UJ \begin{bmatrix} E_{x,in} \\ E_{y,in} \end{bmatrix} = \begin{bmatrix} E_{x,in} \\ E_{y,in} \end{bmatrix}. \tag{5}$$

The AS-CMA algorithm employs a butterfly adaptive filtering structure, which comprises four FIR filters to implement digital polarization demultiplexing, as shown in Fig. 1(c). The output of

Optics EXPRESS

the butterfly filter is given by:

$$\begin{aligned} E'_{x,out}(n) &= \omega_{xx}(n) \cdot E_{x,out}(n) + \omega_{xy}(n) \cdot E_{y,out}(n), \\ E'_{y,out}(n) &= \omega_{yx}(n) \cdot E_{x,out}(n) + \omega_{yy}(n) \cdot E_{y,out}(n). \end{aligned} \tag{6}$$

Here, $E_{x,out}$ and $E_{y,out}$ are the original signals in the x and y polarization states output from the transmission channel, while $E'_{x,out}$ and $E'_{y,out}$ are the signals after polarization recovery and n denotes the sampling index. The symbols $\omega_{xx}, \omega_{xy}, \omega_{yx}, \omega_{yy}$ represent the tap coefficients of the four FIR filters, respectively.

The CMA is a blind equalization technique commonly employed for equalizing constant-envelope signals. It is capable of achieving convergence even in the presence of phase errors. Owing to its computational simplicity, CMA is widely utilized in coherent optical communication systems. At the heart of CMA lies its error function, which is designed to drive the squared modulus of the equalizer's output toward a constant value R_G. Hereafter, the constant R_G is normalized with respect to the instantaneous total power of the signal, thereby enhancing the algorithm's robustness against fluctuations in input signal power.

$$\begin{aligned} e_x(n) &= 1 - \frac{\left|E'_{x,out}(n)\right|^2}{\left|E_{x,out}(n)\right|^2 + \left|E_{y,out}(n)\right|^2}, \\ e_y(n) &= 1 - \frac{\left|E'_{y,out}(n)\right|^2}{\left|E_{x,out}(n)\right|^2 + \left|E_{y,out}(n)\right|^2}. \end{aligned} \tag{7}$$

Typically, the CMA uses a fixed error correction step size. Notice that a large step size is beneficial to the convergence speed, while small step size can reduce the steady-state error. To achieve a balance between the convergence speed and steady-state error, we design an error-driven adaptive variable step size mechanism:

$$\begin{aligned} \mu_x(n) &= \alpha e_x(n) + \beta \left(e_x(n)\right)^2, \\ \mu_y(n) &= \alpha e_y(n) + \beta \left(e_y(n)\right)^2. \end{aligned} \tag{8}$$

During the initial convergence phase, the error $e(n)$ is typically large. This increases the error-driven step size $\mu(n)$, facilitating rapid convergence. As steady-state approaches, the error $e(n)$ decreases and the error-driven step size diminishes accordingly, thereby reducing the steady-state error. The quadratic term $\beta(e(n))^2$ in Eq. (8) boosts the amplification effect of the step size for large errors, further accelerating initial convergence. Here, α and β represent the constant coefficients for the linear and quadratic error terms in the adaptive variable step size, which can be flexibly adjusted based on the target application scenarios.

After optimizing the error correction step size, a simplified sign-based update method was employed instead of standard stochastic gradient descent when updating the filter taps [33]:

$$\begin{aligned} \omega_{xx}(n+1) &= \omega_{xx}(n) + \mu_x(n)\, sgn\{e_x(n)\}\, csgn\left\{E'^{*}_{x,out}(n)\right\} E_{x,out}(n), \\ \omega_{xy}(n+1) &= \omega_{xy}(n) + \mu_x(n)\, sgn\{e_x(n)\}\, csgn\left\{E'^{*}_{x,out}(n)\right\} E_{y,out}(n), \\ \omega_{yx}(n+1) &= \omega_{yx}(n) + \mu_y(n)\, sgn\left\{e_y(n)\right\}\, csgn\left\{E'^{*}_{y,out}(n)\right\} E_{x,out}(n), \\ \omega_{yy}(n+1) &= \omega_{yy}(n) + \mu_y(n)\, sgn\left\{e_y(n)\right\}\, csgn\left\{E'^{*}_{y,out}(n)\right\} E_{y,out}(n), \end{aligned} \tag{9}$$

where the function sgn of the real number x and $csgn$ of complex number z are defined as follows:

$$\begin{aligned} sgn(z) &= \begin{cases} -1 & , z<0 \\ 1 & , otherwise \end{cases}, \\ csgn(z) &= sgn\{Re(z)\} + j\, sgn\{Im(z)\}. \end{aligned} \tag{10}$$

Optics EXPRESS

The sign-based CMA equalizer discards the information about the magnitude and keep only the sign. It effectively simplifies the complex multiplication and reduces the computational complexity. In this case, $sgn\left(e_x\left(n\right)\right)$ determines the direction of tap weight updates and $csgn\left\{E'^{*}_{x,out}\left(n\right)\right\}E_{x,out}\left(n\right)$ extracts the phase of tap weight updates. Although the amplitude information is neglected here, the application of the error-driven adaptive step sizes effectively compensates for this omission. Therefore, the combination of both methods is suitable for high speed real-time systems with computational resource constraints.

To correctly recover the polarization, the four filter taps are orthogonalized as follows:

$$\begin{aligned}
\omega_x\left(n+1\right) &= \left[\omega_{xx}\left(n+1\right) \quad \omega_{xy}\left(n+1\right)\right], \\
\omega_y\left(n+1\right) &= \left[\omega_{yx}\left(n+1\right) \quad \omega_{yy}\left(n+1\right)\right], \\
\omega_x\left(n+1\right) &= \frac{\omega_x(n+1)}{\|\omega_x(n+1)\|}, \\
\omega_y\left(n+1\right) &= \omega_y\left(n+1\right) - \left(\omega_x^H\left(n+1\right)\omega_y\left(n+1\right)\right)\omega_x\left(n+1\right), \\
\omega_y\left(n+1\right) &= \frac{\omega_y(n+1)}{\|\omega_y(n+1)\|},
\end{aligned} \tag{11}$$

where the superscript H denotes the Hermitian transpose. By constrains the norm of the equalizer matrix, the growing or oscillating of the filter taps are avoided and the equalizer can correctly implement the polarization rotation operation, thereby guaranteeing algorithm convergence and system stability.

To further improve the performance of the AS-CMA equalizer, we employ a high-tap-count approach.

$$\begin{aligned}
E'_{x,out}\left(n\right) &= \frac{1}{2k+1}\sum_{m=n-k}^{n+k}\left\{\omega_{xx}\left(n\right)\cdot E_{x,out}\left(m\right) + \omega_{xy}\left(n\right)\cdot E_{y,out}\left(m\right)\right\}, \\
E'_{y,out}\left(n\right) &= \frac{1}{2k+1}\sum_{m=n-k}^{n+k}\left\{\omega_{yx}\left(n\right)\cdot E_{x,out}\left(m\right) + \omega_{yy}\left(n\right)\cdot E_{y,out}\left(m\right)\right\}, \\
e_x\left(n\right) &= 1 - \frac{\left|E'_{x,out}(n)\right|^2}{\left|E_{x,out}(n)\right|^2+\left|E_{y,out}(n)\right|^2}, \\
e_x\left(n\right) &= 1 - \frac{\left|E'_{y,out}(n)\right|^2}{\left|E_{x,out}(n)\right|^2+\left|E_{y,out}(n)\right|^2}.
\end{aligned} \tag{12}$$

In this case, the output for the current symbol is calculated by averaging the filtered outputs over a continuous block of $2k+1$ symbols. This operation effectively smooths out instantaneous fluctuations caused by random noises, thereby providing a cleaner and more stable signal for subsequent error calculation. Furthermore, the average power of the received signal over the corresponding time window is utilized as the normalization reference, which supersedes the inherently unstable instantaneous power benchmark, anchoring the derivation of the error signal to a more dependable local average power. These two improvements suppress the impact of noise on the weight update process, thereby enhancing the algorithm's stability and reducing its steady-state error

There exists an optimal number of taps for a given system. On the one hand, small taps would result in a weak averaging effect and consequently poor algorithm stability with limited performance improvement. On the other hand, large taps introduces excessive filter effect, which degrades its ability to track rapid polarization changes and respond promptly to transient disturbances. Furthermore, the computational complexity increases with taps. Therefore, the optimal number of taps determine on the symbol rate, channel conditions, and real-time processing requirements.

Optics EXPRESS

3. Simulation of AS-CMA based CV-QKD

3.1. 16-APSK CV-QKD

We validate the feasibility of the AS-CMA algorithm in a 16-APSK discrete-modulation CV-QKD simulation system, as shown in Fig. 2. The transmitter (Alice) employs a continuous-wave laser and in-phase/quadrature (I/Q) modulator to implement carrier-suppressed single-sideband (CS-SSB) modulation. The digital modulation signal is generated as follows: (i) Prepare the random number; (ii) Add CAZAC sequence; (iii) Upsampling; (iv) Root-raised-cosine (RRC) pulse shaping; (v) Frequency shift; (vi) Add pilot tone. The symbol rate of the baseband modulated signal is set to 156.25 Mbaud, and the roll-off factor of the RRC filter is 0.3. To mitigate the system's low-frequency noise in practical scenarios, the baseband modulated signal is up-converted by 400 MHz, resulting in a quantum signal center frequency of f_s = 400 MHz. Additionally, a single frequency pilot tone (f_p = 150 MHz) is frequency multiplexed with the quantum signal to estimate the frequency deviation and phase noise between the quantum signal and the local local oscillator (LLO) provided by Bob's independent laser and the polarization impairment.

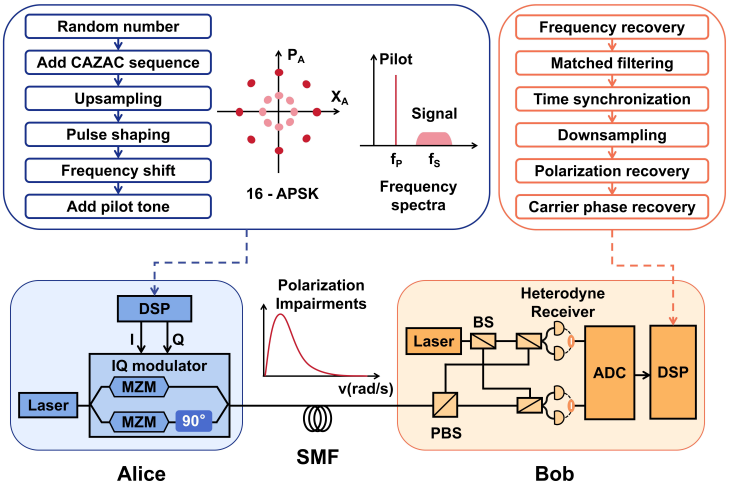

Fig. 2. Schematic of the 16-APSK CV-QKD simulation system.

The variance of the quatnum signal is set to V_A = 1.12, then the quantum signal and the pilot tone are transmitted to Bob via single-mode fiber. During the transmission, polarization rotations are introduced according to the fiber disturbance model described in Section 2.1, and random phase noise is added based on the assumed laser's linewidth of 1 kHz.

At the receiver (Bob), the optical signals exiting the quantum channel is split into X and Y dual-polarizations via a polarization beam splitter (PBS). The LLO frequency is set 50 MHz lower than Alice's laser. Both the quantum signal and pilot tone in X and Y polarizations interfere with the LLO and then detected by heterodyne detectors. The acquired data are then processed via the following procedures: (i) Frequency recovery; (ii) RRC matched filtering; (iii) Time synchronization; (iv) Downsampling; (v) Polarization recovery; (vi) Carrier phase recovery. The recovered quantum signals are then be used to estimate the quantum channel parameters such as T, ξ_A, and the SKR. The signal-to-noise ratio (SNR) of the pilot tone used for polarization

Optics EXPRESS

and phase recovery is approximately 16 dB after the downsampling at 50 km single-mode fiber transmission.

3.2. Simulation results and analysis

To comprehensively evaluate the polarization recovery performance of the AS-CMA algorithm in CV-QKD systems, we focuses on three core metrics: T, ξ_A, and SKR. The T directly reflects quantum signal transmission efficiency, and ξ_A indicates the system security, while the SKR serves as the benchmark for assessing the overall performance of QKD systems.

3.2.1. Performance comparisons analysis of different CMA algorithms on 25 km and 50 km fiber channels

To comprehensively evaluate the robustness of the proposed algorithm, comparative tests were conducted under two different single-mode fiber length: 25 km (linear loss of 5 dB) and 50 km (linear loss of 10 dB). As shown in Fig. 3(a)-f, although increased channel loss caused an overall decline in performance metrics (T, ξ_A, and SKR) for all three algorithms, C-CMA, AS-CMA$_1$ (taps=1), and AS-CMA$_{33}$ (taps=33), they exhibited distinct gradations in performance degradation. Among them, the AS-CMA$_{33}$ algorithm presents significant superiority at both transmission distances.

As shown in Fig. 3(a), in a 25 km channel, when the SOP rotation rate increases to 10 Mrad/s, the T value with the C-CMA algorithm declines from 0.315 to 0.224 (a 28.9% decrease). The AS-CMA$_1$ algorithm effectively mitigates performance degradation using adaptive step size, maintaining T at 0.282. The AS-CMA$_{33}$ algorithm, combining adaptive step size with high taps, demonstrates optimal results, suppressing the decline of T within 4.1% (0.302). This advantage becomes more evident in a 50 km channel (Fig. 3(d)): The T value with the C-CMA algorithm decreases from 0.099 to 0.041. While the AS-CMA$_1$ algorithm significantly outperforms C-CMA, the AS-CMA$_{33}$ algorithm shows only a minor decrease of 5.1% (from 0.099 to 0.094), demonstrating its robustness against disturbances.

The impact of the polarization rotation to the excess noises are shown in Fig. 3(b) and 3e. At 25 km and SOP rotation rate of 10 Mrad/s, the excess noise ξ_A increase to 39.79, 23.54, and 10.08 mSNU, for the C-CMA, AS-CMA$_1$, and AS-CMA$_{33}$, respectively. For longer distance of 50 km, the corresponding excess noises are 52.92, 30.95, and 20.48 mSNU respectively. Above results demonstrate the superior noise control capability of the AS-CMA$_{33}$.

Figure 3(c) and 3f depict the system's SKR, which characterizes the overall performance. Over a 25 km channel, under strong interference of up to 10 Mrad/s, the SKR using the C-CMA algorithm declines sharply by 77.9%, dropping to 1.36 Mbps. In comparison, the AS-CMA$_1$ algorithm enhances the SKR to 3.50 Mbps. The AS-CMA$_{33}$ algorithm demonstrates the highest robustness, maintaining a high SKR of 5.38 Mbps with only a 12.9% reduction. For 50 km channel, the C-CMA algorithm could no longer generate positive secret keys at 10 Mrad/s; while the AS-CMA$_{33}$ and AS-CMA$_1$ can still support key rate of 0.928 and 0.526 Mbps, respectively.

Figure 4 plots the SKR versus the SOP rotation rate for the AS-CMA$_{33}$ algorithm at different single-mode fiber lengths. It presents the maximum tolerable SOP rotation rate at which the AS-CMA$_{33}$ algorithm can maintain a positive SKR across different transmission distances. The tolerable rotation rate decreases with increasing distances: from above 100 Mrad/s at 10 km gradually drops to 40 Mrad/s at 50 km. Because longer transmission distance means higher channel loss, which increase the sensitivity of the QKD system to the polarization disturbance.

Notice that the symbol rate also affects the tolerable SOP rotation rate. A higher symbol rate shortens the symbol period, thereby alleviating the burden on the channel tracking. However, SOP rotation leads to broadening of the spectrum of both the pilot tone and quantum signal. The bandwidth constraints imposed by both the matched filtering of the quantum signal and the

Optics EXPRESS

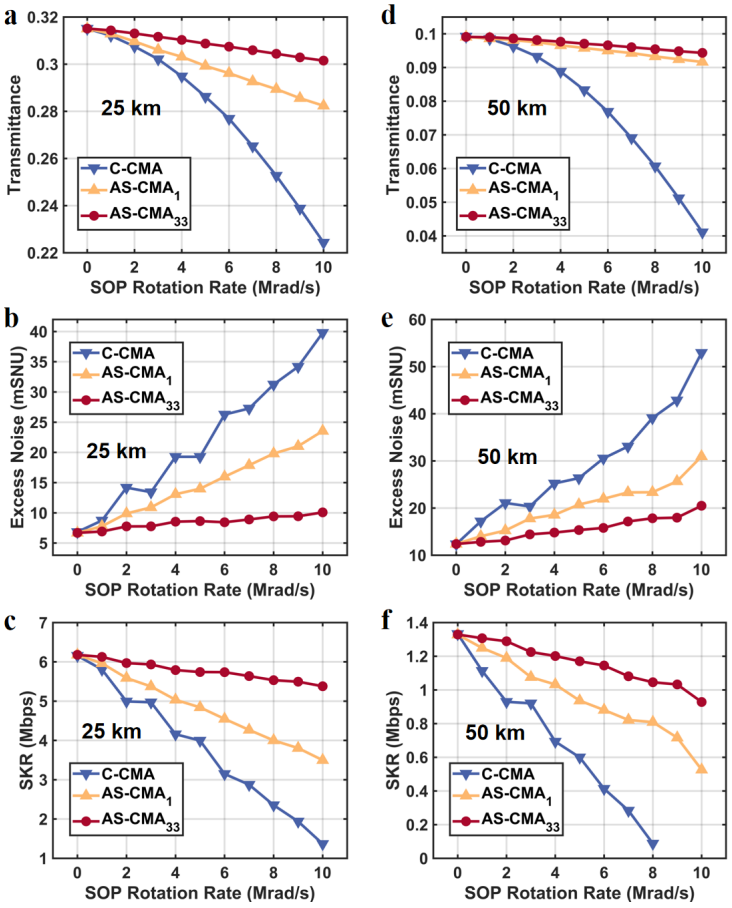

Fig. 3. Performance comparison of different CMA algorithms in CV-QKD at varying SOP rotation rates. The system performance is evaluated over 25-km and 50-km single-mode fiber. (a),(d) Transmittance of the quantum channel T; (b),(e) Excess noise ξ_A; (c),(f) SKR.

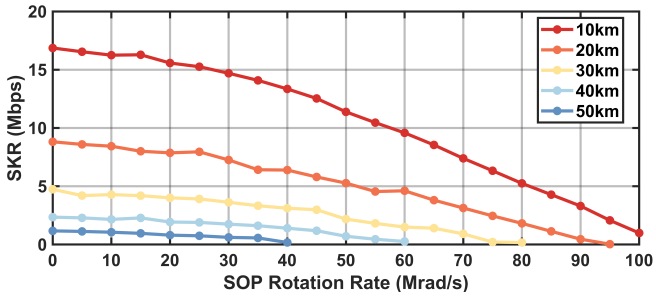

Fig. 4. SKR as a function of SOP rotation rate under various single-mode fiber lengths for the AS-CMA$_{33}$ algorithm.

Optics EXPRESS

low-pass filtering of the pilot signal cause the tolerable SOP rotation rate to exhibit diminishing gains and eventual saturation as the symbol rate increases.

3.2.2. Dynamic response under lightning disturbance

Finally, we construct a lightning strike model to test the algorithm's dynamic response under extreme polarization disturbances. The typical lightning strike features a primary peak of 43 Mrad/s and a secondary peak of 12 Mrad/s occurring within 40 μs, as shown in Fig. 5. The adaptive step size μ of the AS-CMA$_{33}$ tracks changes of the error e in real time with high sensitivity. In the initial data recovery phase, the error value rapidly convergence in just 8 iterations. During polarization disturbance peaks, the step size scales up with the error e, thereby accelerating convergence. After the disturbance peaks subside, the step size is quickly reduced in response to the error e, enabling high steady-state accuracy.

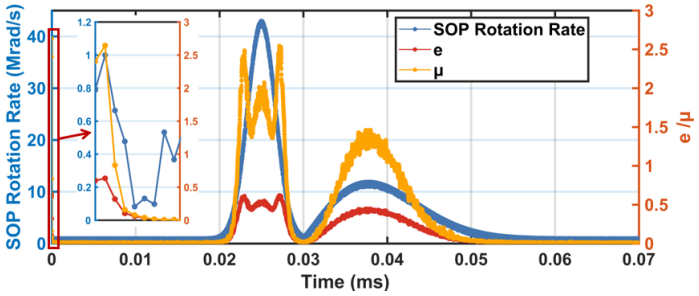

Fig. 5. Dynamic response of the AS-CMA$_{33}$ algorithm under lightning strikes.

Table 1 shows the simulated performance of the CV-QKD with and without the lighting strikes, including the estimated quantum channel transmittance T, excess noise ξ_A, and the SKR. In our simulation, the block length of symbols used for parameter estimation is 1.5625 M (corresponding to a 10 ms transmission time for a 156.25 MBaud system). Within each block we assume that one complete lightning strike event occurs. This block length ensures the statistical reliability of parameter estimation while preventing the impact of the lightning strike from being averaged out over a longer period. Furthermore, all results presented in Table 1 are obtained by averaging over 50 independent simulation runs, ensuring the credibility of the performance evaluation. The presence of lightning strikes leads to a marginal degradation in the estimated channel transmittance and a slight elevation in excess noise. These combined effects result in a reduction of less than 7% in SKR for the CV-QKD system at both 25 km and 50 km. This result demonstrates that the proposed algorithm not only maintains robust performance under continuous polarization disturbances but also effectively handles extreme, sudden disturbances such as lightning strikes.

Table 1. Performance of the CV-QKD with and without lightning strikes.

	25km		50km	
	without lightning strikes	with lightning strikes	without lightning strikes	with lightning strikes
T	0.3130	0.3126	0.09852	0.09842
ξ_A (mSNU)	9.129	11.736	15.567	17.305
SKR (Mbps)	5.771	5.410	1.181	1.107

Optics EXPRESS

3.2.3. Simulation analysis of a polarization division multiplexing 16-APSK CV-QKD system

In this section, we further simulated a polarization division multiplexing (PDM) LLO CV-QKD system to validate the performance of the AS-CMA algorithm. In this system, a continuous-wave laser at Alice is split into two beams and each beam is independently modulated by an I/Q modulator. The two quantum signals share the same frequency band while are orthogonally polarized (X and Y polarization states). Two frequency-division multiplexed pilot tones are introduced to assist in the polarization and phase recovery of the quantum signals. At Bob's side, a receiver similar to that in Fig. 2 is employed.

Figure 6 shows the SKR versus the SOP rotation rate at different single-mode fiber lengths for the X and Y polarization signals in the PDM system. The simulation results validate the effectiveness and robustness of the AS-CMA algorithm in polarization multiplexing scenarios. We see that the variation of SKR with the increasing SOP rotation rate in the PDM system is similar to that in the single polarization system. In the PDM system, while the AS-CMA can recover both polarization signals simultaneously, the recovery performance for each is somewhat compromised. This is due to the polarization crosstalk effect, which results in a decrease in SKR.

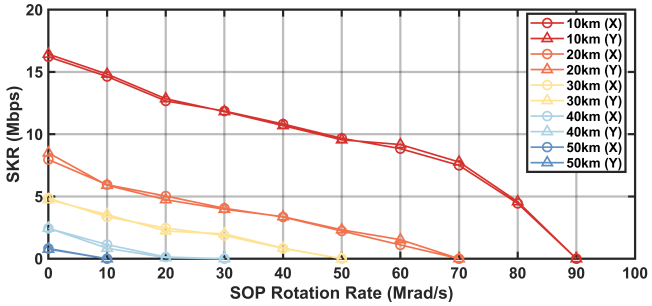

Fig. 6. SKR as a function of SOP rotation rate under various single-mode fiber lengths for the AS-CMA algorithm in a PDM CV-QKD system.

4. Conclusion

In summary, we designed an AS-CMA algorithm that combines high convergence efficiency, low computational cost, and strong robustness. It employs an error-driven adaptive stride mechanism to dynamically trade off convergence speed against steady-state error. Simultaneously, it leverages a sign-based weight update method to lower computational complexity, making the algorithm well-suited for communication systems with real-time demands. The effectiveness of the algorithm is evaluated on a 16-APSK CV-QKD simulation system. Simulation results validate the algorithm's superior performance. In future work, we will focus on implementing the proposed algorithm on an FPGA hardware platform to enable real-time processing.

Funding. National Natural Science Foundation of China (62205188, 62175138); Quantum Science and Technology-National Science and Technology Major Project (2021ZD0300703).

Disclosures. The authors declare no conflicts of interest.

Data Availability. Data underlying the results presented in this paper are not publicly available at this time but may be obtained from the authors upon reasonable request.

References

1. F. Xu, X. Ma, Q. Zhang, *et al.*, "Secure quantum key distribution with realistic devices," Rev. Mod. Phys. **92**(2), 025002 (2020).
2. S. Pirandola, U. L. Andersen, L. Banchi, *et al.*, "Advances in quantum cryptography," Adv. Opt. Photonics **12**(4), 1012–1236 (2020).
3. J. N. Damask, *Statistical Properties of Polarization in Fiber* (Springer, 2005), pp. 385–428.

Optics EXPRESS

4. Y. Feng, L. Li, J. Lin, *et al.*, "Joint tracking and equalization scheme for multi-polarization effects in coherent optical communication systems," Opt. Express **24**(22), 25491–25501 (2016).
5. N. Cui, X. Zhang, Z. Zheng, *et al.*, "Two-parameter-SOP and three-parameter-RSOP fiber channels: problem and solution for polarization demultiplexing using Stokes space," Opt. Express **26**(16), 21170–21183 (2018).
6. D. Xu, O. Lopez, A. Amy-Klein, *et al.*, "Polarization scramblers to solve practical limitations of frequency transfer," J. Lightwave Technol. **39**(10), 3106–3111 (2021).
7. K. Hu, F. Tong, W. Lian, *et al.*, "Model and experimental verification of SOP transient in OPGW based on direct strike lightning," Opt. Express **31**(23), 39102–39120 (2023).
8. F. Tong, K. Hu, W. Li, *et al.*, "Measurement of optical signal state of polarization in OPGW under lightning strike condition," in *Optical Fiber Communication Conference*, (Optica Publishing Group, 2024), pp. W2B–5.
9. D. Charlton, S. Clarke, D. Doucet, *et al.*, "Field measurements of SOP transients in OPGW, with time and location correlation to lightning strikes," Opt. Express **25**(9), 9689–9696 (2017).
10. P. M. Krummrich, D. Ronnenberg, W. Schairer, *et al.*, "Demanding response time requirements on coherent receivers due to fast polarization rotations caused by lightning events," Opt. Express **24**(11), 12442–12457 (2016).
11. Y. Zhang, Y. Bian, Z. Li, *et al.*, "Continuous-variable quantum key distribution system: Past, present, and future," Appl. Phys. Rev. **11**(1), 011318 (2024).
12. J. Ma, D. Qi, L. Cui, *et al.*, "Enhanced-rate continuous-variable quantum key distribution with particle filter-based carrier phase recovery," Opt. Express **33**(22), 47178–47193 (2025).
13. A. A. Hajomer, I. Derkach, N. Jain, *et al.*, "Long-distance continuous-variable quantum key distribution over 100-km fiber with local local oscillator," Sci. Adv. **10**(1), eadi9474 (2024).
14. Y. Tian, P. Wang, J. Liu, *et al.*, "Experimental demonstration of continuous-variable measurement-device-independent quantum key distribution over optical fiber," Optica **9**(5), 492–500 (2022).
15. F. Roumestan, A. Ghazisaeidi, J. Renaudier, *et al.*, "Shaped constellation continuous variable quantum key distribution: Concepts, methods and experimental validation," J. Lightwave Technol. **42**(15), 5182–5189 (2024).
16. Y. Xu, X. Liao, Q. Zhang, *et al.*, "OFDM-based quantum key distribution access network reaching Nyquist limits," Optica **12**(10), 1668–1680 (2025).
17. H. Yin, P. Huang, Z. Zhou, *et al.*, "All-day free-space quantum key distribution with thermal source towards quantum secure communications for unmanned vehicles," npj Quantum Inf. **11**(1), 134 (2025).
18. Y. Pan, Y. Bian, Y. Li, *et al.*, "High-rate 16-node quantum access network based on a passive optical network," Optica **12**(7), 953–960 (2025).
19. S. Liu, Y. Tian, Y. Zhang, *et al.*, "Integrated quantum communication network and vibration sensing in optical fibers," Optica **11**(12), 1762–1772 (2024).
20. S. Liu, Z. Lu, P. Wang, *et al.*, "Experimental demonstration of multiparty quantum secret sharing and conference key agreement," npj Quantum Inf. **9**(1), 92 (2023).
21. Y. Tian, Y. Zhang, S. Liu, *et al.*, "High-performance long-distance discrete-modulation continuous-variable quantum key distribution," Opt. Lett. **48**(11), 2953–2956 (2023).
22. S. Liu, Y. Zhang, S. Ren, *et al.*, "Experimental demonstration of complete quantum e-commerce based on an efficient quantum digital payment," Photonics Res. **13**(3), 572–582 (2025).
23. W. Liu, Y. Cao, X. Wang, *et al.*, "Continuous-variable quantum key distribution under strong channel polarization disturbance," Phys. Rev. A **102**(3), 032625 (2020).
24. Z. Li, X. Wang, D. Qi, *et al.*, "High-speed implementation of continuous-variable quantum key distribution with polarization multiplexing," J. Lightwave Technol. **44**(1), 47–55 (2026).
25. T. Wang, P. Huang, S. Wang, *et al.*, "Polarization-state tracking based on Kalman filter in continuous-variable quantum key distribution," Opt. Express **27**(19), 26689–26700 (2019).
26. T. Shen, X. Wang, Z. Chen, *et al.*, "Experimental demonstration of LLO continuous-variable quantum key distribution with polarization loss compensation," IEEE Photonics J. **15**(6), 1–8 (2023).
27. J. Jignesh, B. Corcoran, C. Zhu, *et al.*, "Unscented Kalman filters for polarization state tracking and phase noise mitigation," in *optical fiber communication conference*, (Optical Society of America, 2016), pp. 1–3.
28. H.-M. Chin, A. A. Hajomer, N. Jain, *et al.*, "Machine learning based joint polarization and phase compensation for CV-QKD," in *Optical Fiber Communication Conference*, (Optica Publishing Group, 2023), pp. Th3J–2.
29. Y. Pan, H. Wang, Y. Shao, *et al.*, "Simple and fast polarization tracking algorithm for continuous-variable quantum key distribution system using orthogonal pilot tone," J. Lightwave Technol. **41**(19), 6169–6175 (2023).
30. J. Li, T. Zeng, X. Li, *et al.*, "Real-time fast polarization tracking based on polarization phase locking least mean square algorithm," Opt. Express **27**(16), 22116–22126 (2019).
31. P. Yi, D. Li, H. Song, *et al.*, "Experimental investigation on low-complexity adaptive equalizer including RSOP tracking and phase recovery for 112 Gb/s PDM-QPSK transmission system," IEEE Photonics J. **13**(2), 1–15 (2021).
32. B. Koch, R. Noé, and V. Mirvoda, "Time-resolved Mueller matrix measurement and polarization scrambler characterization," in *2016 21st European Conference on Networks and Optical Communications (NOC)*, (IEEE, 2016), pp. 168–173.
33. M. S. Faruk and S. J. Savory, "Digital signal processing for coherent transceivers employing multilevel formats," J. Lightwave Technol. **35**(5), 1125–1141 (2017).